Applied Energy 382 (2025) 125199

Contents lists available at ScienceDirect

Applied Energy

journal homepage: www.elsevier.com/locate/apenergy

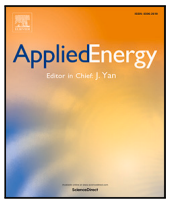

Dynamic mass and energy balance model of a 50 kW proton exchange membrane electrolyzer system

Georgios Sakas [a,*], Philipp Rentschler [b], Antti Kosonen [a], Peter Holtappels [b], Vesa Ruuskanen [a], Pertti Kauranen [a], Jero Ahola [a], Roland Dittmeyer [b]

[a] Lappeenranta–Lahti University of Technology LUT, P.O. Box 20, FI-53851, Lappeenranta, Finland
[b] Karlsruhe Institute of Technology, Karlsruhe, Germany

ARTICLE INFO

Keywords:
Industrial-scale
Green hydrogen
Water electrolysis
PEM
Modeling
Simulation

ABSTRACT

This paper presents a parameter-adjustable dynamic mass and energy balance process model for a 50 kW proton exchange membrane (PEM) electrolyzer plant. Energy and mass balances are derived for the electrolyzer stack, heat exchangers, and gas–liquid separation vessels. These balances, along with semiempirical submodels, are integrated and solved within MATLAB system blocks connected through a Simulink environment. The model is validated using experimental data obtained from a comparable industrial plant with similar pressure, power, and system design parameters. The PEM plant is capable of operating within a pressure range of 5–55 bar. The electrochemical and thermal behaviors, along with hydrogen production, are compared between the process model and the actual PEM plant to assess the accuracy of the simulations. The results demonstrate a satisfactory agreement between the model predictions and experimental data. In nominal operation, 68.5% of the total power supplied to the stack is converted into hydrogen, while the remaining power is dissipated as heat due to overvoltages. This excess heat is primarily transferred through the heat exchangers to the secondary leg.

1. Introduction

Hydrogen is primarily used in heavy industries for crude oil refining, ammonia production, and methanol synthesis, accounting for 93% of the total hydrogen consumption. Presently, the main method of hydrogen production involves the use of fossil fuels. However, the emergence of green hydrogen (GH2) offers a promising alternative to mitigate environmental impacts. GH2 is derived from renewable energy sources (RES) and is labeled as the fuel of the future. Its distinction lies in being both clean and easily storable, making it a compelling solution for sustainable energy needs. While the current use of hydrogen is centered around heavy industries, GH2 is designed to extend its application beyond this sector. Its intended use spans various applications, including aviation, maritime transport, and energy [1].

Low-temperature electrolyzers, specifically the proton exchange membrane (PEM) and the alkaline water electrolyzer (AWE), stand out as two technologically mature options for industrial-scale GH2 production. These electrolyzers use the water electrolysis reaction to produce high-purity GH2. Among the two, the AWE is more mature and widely adopted than the PEM, owing to its advantages of low-cost catalysts and a prolonged lifespan. However, the AWE faces limitations in terms of achievable current density compared with the PEM. Despite this advantage, PEM electrolyzers use expensive catalysts like platinum and iridium, which could limit their scalability for larger production [2].

This paper will focus on commercial-size PEM electrolyzer plant modeling, including the stack and essential peripheral unit operations. So far, the literature has focused on characterizing the electrochemical and thermal behavior at the cell/stack level [3]. Additionally, there is a scarcity of literature on the simulation and modeling of PEM water electrolyzer systems that provide detailed characterization of commercial-size systems that include all the important peripheral components, such as gas–liquid separation vessels, heat exchangers, and pumps. To fill this research gap, in this work, a commercial 50 kW PEM water electrolyzer system is modeled and validated with experimental data from an analogous operating system, aiming to provide a numerical tool to investigate the dynamic performance and energy efficiency of such systems.

Examining the published research work on the simulation and modeling of PEM water electrolyzer systems, Yigit and Selamet [4] performed a simulation for a PEM system with the target of understanding how the stack and the overall system perform and experience inefficiencies under varying operating conditions. The simulation relied on mathematical models solved by using MATLAB/Simulink software.

* Corresponding author.
E-mail address: Georgios.Sakas@lut.fi (G. Sakas).

https://doi.org/10.1016/j.apenergy.2024.125199
Received 26 April 2024; Received in revised form 15 October 2024; Accepted 19 December 2024
Available online 1 January 2025

Nomenclature

Acronyms

AC	Alternating current
AWE	Alkaline water electrolyzer
DC	Direct current
GH2	Green hydrogen
HE	Heat exchanger
IGBT	Insulated gate bipolar transistors
ODE	Ordinary differential equation
PEM	Proton exchange membrane
PSU	Power supply unit
PtX	Power to x
RES	Renewable energy sources
SEC	Specific energy consumption

Variables

ΔH	Higher heating value
$\dot{m}$	Mass flow rate
$\dot{n}$	Molar flow rate
$\dot{Q}$	Heat flow
A	Surface area
C	Thermal capacitance
D	Diameter
F	Faraday constant
H	Height
h	Heat transfer coefficient
I	Current
i	Current density
K	Darcy coefficient
k	Thermal conductivity
L	Length
M	Molar mass
N	Number
n	Coefficient
P	Pressure
p	Model parameter
q	Heat transfer rate
R	Gas constant
r	Model parameter
s	Model parameter
T	Temperature
t	Model parameter
t	Time
U	Voltage
V	Volume
z	Moles of electrons transferred
Cp	Specific heat
Nu	Nusselt number
Pr	Prandtl number
Re	Reynolds number
Δ	Difference
δ	Thickness
η	Efficiency
λ	Latent heat
μ	Viscosity
ρ	Density
Σ	Sum
σ	Stefan–Boltzmann constant
τ	Time constant

Subscript

A	Stack A
act	Activation
amb	Ambient
an	Anode
B	Stack B
c	Cell
cat	Cathode
cd	Cold
cn	Concentration
con	Consumed
cv	Convection
cw	Cooling water
ef	Effective
eo	Electroosmotic
F	Faraday
gen	Generated
h	Hot
hc	Hydrogen crossover
in	Inlet
init	Initial
liq	Liquid
m	Membrane
mp	Makeup water
net	Equilibrium
oc	Oxygen crossover
ohm	Ohmic
out	Outlet
pe	Pressure effect
pp	Pump
rd	Radiation
rev	Reversible
s	Stack
s,H_2	Hydrogen gas separation
s,O_2	Oxygen gas separation
s,l	Liquid separation
sec	Secondary
SP	Set-point
sur	Surface
tn	Thermoneutral
v	Vapor
vap	Vaporization
w	Water

The stack design in the simulation was considered to comprise five cells with an active area of $100\,cm^2$. The study presented several findings: (1) Notably, the anodic activation losses and the ohmic losses caused by ionic resistance were considerably greater than the electronic and cathodic activation losses. (2) Elevating the operational pressure led to an increase in the stack voltage, coinciding with a reduction in the overall stack efficiency. (3) Raising the operational temperature, conversely, lowered the polarization curve of the stack, resulting in an enhanced overall stack efficiency. (4) Alterations in temperature had a more pronounced impact on cell voltage than pressure changes. (5) Lastly, the research compared the losses of the stack with the losses

in the power supply, pump, fan, controller, and sensors. In all cases of current densities, the stack losses surpassed the losses of the other components. However, at lower current densities, the difference in stack and other component losses was less significant compared with higher current densities.

Expanding the research field of modeling PEM water electrolyzer systems, Espinosa et al. [5] developed a model for a high-pressure 46 kW PEM water electrolyzer system, which they validated using a real-scale demonstration. The entire model was built in Matlab-Simulink, and several experiments were conducted at different temperatures and loads to align the modeled electrochemical behavior with that of the real system. Their analysis showed that high temperature and low pressure operating conditions improve electrolyzer efficiency. Continuing along the same lines, Ni et al. [6] constructed a model for a PEM electrolyzer plant to investigate its energy and exergy efficiency. The model was validated by using polarization curve data extracted from Ioroi et al. [7]. The modeled plant included a single PEM stack, a heat exchanger, and an oxygen separation unit. The findings of the study suggest that the energy efficiency of the plant can be enhanced by using a thinner PEM electrolyte and increasing the temperature of the operating process.

Hancke et al. [8] analyzed the results from experimental testing of a 12 kW PEM water electrolyzer system. The research focused on investigating the effect of pressure on electrolyzer performance and discussing the trade-off between stack and system efficiency. The case studies considered scenarios where downstream mechanical compression loss is reduced due to high-pressure stack operation. The study confirmed that high-pressure PEM stacks have diminished performance, particularly above 30 bar, with a significant drop occurring over 100 bar. It also revealed that high-pressure PEM water electrolyzer systems consume more energy compared to state-of-the-art electrolyzer systems with mechanical compression. However, the business case remains open, and further techno-economic optimization studies are needed to determine the trade-off between systems that combine low-pressure stack operation with high mechanical compression loss and those that combine high-pressure stack operation with reduced mechanical compression loss.

Pfennig et al. [9] developed an initial model of megawatt-size PEM water electrolyzer systems. Since the authors did not have access to industrial measurements, the model was built using parameters from the literature and operational points from published commercial PEM stacks. The study aimed to introduce a preliminary approach to modeling such systems. However, the model only investigated the performance of the stack, excluding the peripheral components. The authors also noted that there are hardly any corresponding system models of this size in the literature that dynamically simulate the performance of commercial-scale PEM water electrolyzer systems.

1.1. Aim of the study

Summarizing prior research on PEM electrolyzer plant modeling, it is evident that there is a scarcity of research articles addressing commercial- or industrial-scale PEM water electrolyzers as a complete plant process, including all essential peripheral unit operations. The majority of modeling articles in the field of PEM electrolyzers tend to concentrate on characterizing the electrochemical and thermal behavior of the stack, rather than considering the system at a holistic level [3]. Moreover, these studies typically focus on small-scale and single-cell applications within the watt range. Furthermore, verification is typically carried out using a single polarization curve at a fixed temperature. Similar observations were reported from Espinosa-Lopez et al. [5] literature review, indicating that while research on PEMWE is extensive, there is limited work on modeling commercial-scale PEM plant systems that also include all the important peripheral components, not only the cell or stack.

The novel contributions of our study concerning the PEM electrolyzer plant modeling are summarized as follows:

Table 1
Technical characteristics of the experimental 50 kW plant. The voltage range is estimated during operation at a constant temperature of 60 °C.

Parameter	Value	Unit
Number of stacks	2	–
Number of cells per stack	40	–
Stack length	98	cm
Stack height	25	cm
Stack width	35	cm
Active cell area	875	cm^2
Maximum operating pressure	55	bar
Maximum operating temperature	90	°C
Operating cell block current range	0–300	A
Maximum allowable cell block current	750	A
Cell block voltage range	1.27–2.16	V
Total stack voltage range	50.8–86.4	V
Separation tank volume	15.2	L

- The study presents a dynamic mass and energy balance model methodology to simulate a 50 kW PEM electrolyzer plant process.
- The overall process model incorporates several sub-models for all unit operations within the PEM system, including stack, gas–liquid separation vessel, and heat exchanger sub-models. In addition, the energy and mass balance for each unit operation are derived and presented in this work.
- Measurements from a commercial 50 kW PEM electrolyzer plant were collected.
- The measurements were used to build, configure and verify the dynamic process model. Specifically, multiple measured polarization curves at various temperatures were used to fit the operational polarization curve to the model. Additionally, verification was performed at multiple dynamic levels, including stack temperature, plant hydrogen production, and H_2inO_2 impurities. These parameters were compared between the operational plant and the model to ensure the accuracy of the dynamic simulation.
- The main contribution of this research is the utilization of the verified 50 kW commercial-scale PEM water electrolyzer process model to investigate the performance and energy efficiency of such systems. Mainly, the stack heat balance and SEC are analyzed, and the energy flow across the plant is illustrated using a Sankey diagram.

The remainder of the publication is structured as follows: Section 2 describes the experimental PEM plant process used to gather the necessary data. Section 3 presents the dynamic process model and outlines the methodology. Section 4 elaborates on the model verification and discusses the results of the study. Section 5 contains conclusions, providing a summary of the article and highlighting the main findings.

2. Plant process of proton exchange membrane electrolysis

The PEM electrolyzer plant under investigation is manufactured in 2013. In Fig. 1, a simplified version of the process diagram for the experimental setup is presented. The system consists of a total of four PEM stacks, each with a capacity of 25 kW and 100 kW in total. For short-term peak loads, the system can be operated at 300 kW for a maximum of 15 min, whereby the maximum current per cell block is limited to 750 A ($0.857\,A\,cm^{-2}$) and the maximum cell block voltage to 120 V DC. In this study, half of the system, i.e., two stacks, were operated. As a result, the nominal power supply for the process is 50 kW. The technical characteristics of the experimental setup are shown in Table 1.

2.1. Process diagram description

As shown in Fig. 1, the PEM electrolyzer plant typically employs alternating current (AC), initially directed to the power supply unit.

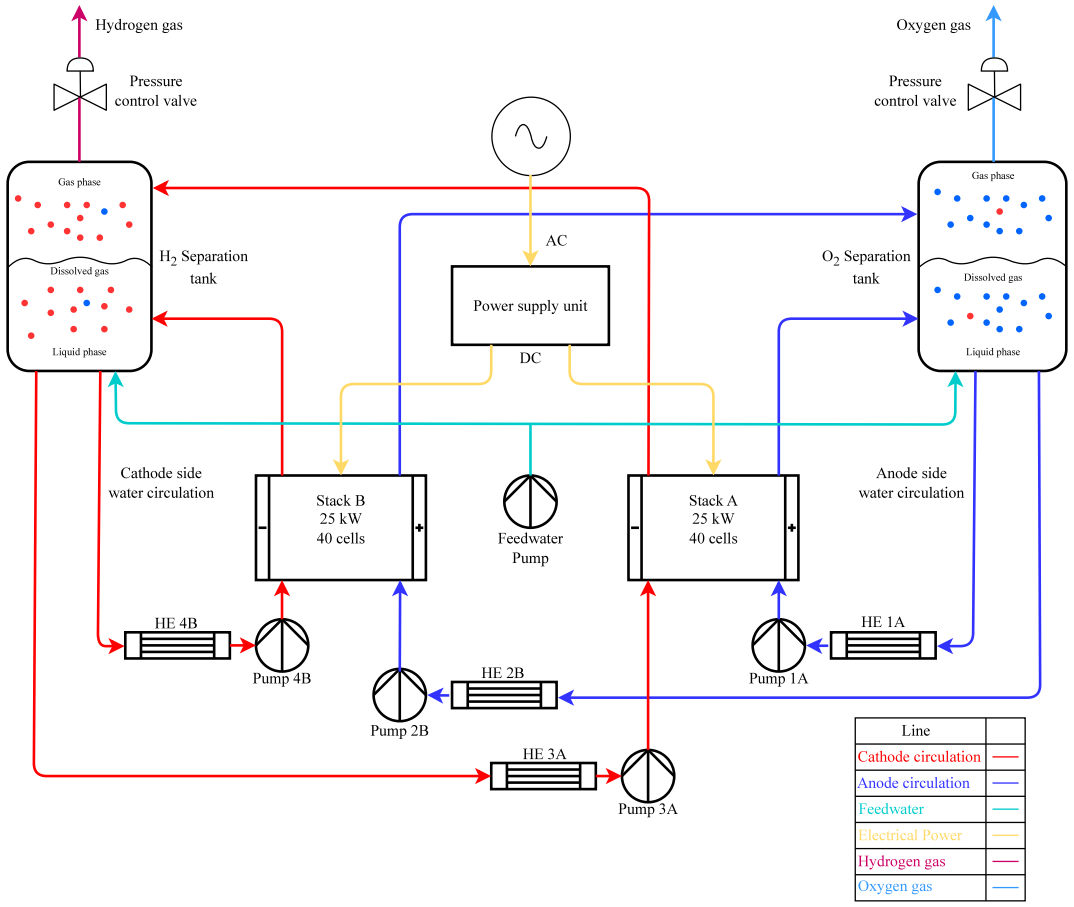

Fig. 1. Plant diagram of the experimental setup. In the cathode and anode circulation lines, the cathode line carries a two-phase flow of hydrogen gas mixed with water and a small fraction of oxygen gas (impurities), while the anode line carries a two-phase flow of oxygen gas and water with a small fraction of hydrogen gas (impurities).

The AC electric current is converted into direct current (DC) with a transformer and rectifiers. The three common rectifier topologies for industrial-scale water electrolysis are 6-pulse and 12-pulse thyristor rectifiers and buck rectifiers based on insulated gate bipolar transistors (IGBT) [10,11]. In continuation, the DC current, along with AC ripple [12], is supplied to both stack A and stack B, converting the water into hydrogen molecules at the catalyst surface of the cathode electrode and into oxygen molecules at the catalyst surface of the anode electrode by the water splitting reaction [9,13]. Each stack is constructed of 40 cells connected electrically in series. The electrolyzer can be operated up to a maximum pressure of 55 bar. The pressure is regulated by the gas outlets, and there is the same pressure at the anode and the cathode, which reduces the mechanical load on the membrane.

The produced hydrogen and oxygen gases exit the stacks as a two-phase flow of water and gas, flowing into their respective hydrogen and oxygen separation tanks. The vertical gas–liquid separation tanks of 15.2 L volume employ gravity mechanisms to separate the gas phase from the liquid phase [14]. The gas remains in the upper tank area, and the liquid settles in the lower tank area. The separated hydrogen gas is typically stored in an outer storage vessel until use, while the oxygen gas is released into the atmosphere. However, the use or storage of the produced hydrogen and oxygen gases is beyond the scope of this study, and the gases are vented into the atmosphere.

The liquid from the lower section of the separation tanks circulates back to the stacks with the assistance of centrifugal pumps. Centrifugal pumps serve two main purposes. First, they regulate the mass flow rate necessary to maintain circulation in the closed loop. Secondly, they ensure the system efficiency by facilitating the removal of produced gases from the stack. Additionally, in connection with heat exchangers, they control the cooling of the stack and the peripheral units [15]. Before re-entering the stack, the liquid undergoes a cooling process to achieve the desired temperature. This cooling takes place in heat exchangers and is crucial for regulating the thermal behavior of the stack. The heat generated by overpotential losses within the stack can accumulate, requiring extraction from both the stack and associated unit operations in the circulation loop.

3. PEM plant modeling

In this section, the methodology for stack- and system-level modeling is presented and explained in detail. The stack-level model consists primarily of electrochemical, thermal, and mass transfer models. The system-level modeling incorporates the main unit operations dynamically connected in MATLAB Simulink. These unit operations include: (1) stack; (2) hydrogen–liquid separation tank; (3) oxygen–liquid separation tank; and (4) heat exchangers. Furthermore, the model methodology for each unit is presented and discussed.

3.1. Stack hydrogen production

The total hydrogen production rate in a water electrolysis stack, whether for the AWE or the PEM, is directly proportional to the supplied DC current and can be estimated as follows [16]:

$$\dot{n}_{H_2} = \left(\eta_F \cdot \frac{i_c \cdot A_{ef}}{z \cdot F}\right) \cdot N_c, \tag{1}$$

where i_c represents the current density, A_{ef} stands for the effective/active cell area, z denotes the number of moles of electrons transferred in the reaction (which is two for hydrogen), F represents the Faraday constant, N_c is the total number of cells electrically

connected in series in the stack, and η_F is the Faraday/current efficiency of the stack.

Current efficiency η_F losses are primarily caused by shunt currents. The manifold ducts within the stack can introduce additional resistance paths, through which a portion of the supplied current may flow [17]. These shunt currents lead to corrosion of the manifold ducts and result in the loss of current through secondary electrochemical reactions. Shunt currents are commonly observed in industrial-scale AWE stacks manufactured as a bipolar configuration [18] owing to the geometric design and the use of circulating conductive electrolyte. On the other hand, PEM water electrolyzer stacks circulate highly resistive water and typically do not exhibit a high level of shunt currents, and thus, an assumption is often made that the current efficiency is 100%. Nevertheless, in this study, the current efficiency is not assumed to be 100%. This approach allows us to examine the validity of the commonly used assumption.

3.2. Electrochemical model

The electrochemical reaction in water electrolyzer stacks occurs relatively fast compared with other physical phenomena. Therefore, a static characteristic model is sufficient for predicting system-level performance, allowing us to ignore the details of electrochemical processes [19]. The overall cell voltage U_c can be expressed as the sum of the reversible voltage U_{rev} and additional overvoltages, namely the activation U_{act}, ohmic U_{ohm}, and concentration overvoltages U_{cn} [20]:

$$U_c = U_{rev} + U_{act} + U_{ohm} + U_{cn}. \tag{2}$$

Concentration overvoltages primarily occur at high current densities because of mass transfer limitations. In our case, the current density is relatively low, 0.34 A cm^{-2}, at the nominal operating point, allowing us to disregard concentration overvoltages.

3.2.1. Reversible voltage

The reversible voltage represents the minimum electrochemical potential required for the water splitting reaction to occur. It depends on thermodynamic properties, such as pressure and temperature, and can be estimated using the Nernst equation as follows [12]:

$$U_{rev} = U^0_{rev} + \frac{R \cdot T}{2 \cdot F} \cdot \ln\left(\frac{(P_{cat} - P_{v,w}) \cdot (P_{an} - P_{v,w})^{1/2}}{P_{sd}^{3/2}}\right). \tag{3}$$

$$U_{rev} = U^0_{rev} + \frac{R \cdot T}{2 \cdot F} \cdot \ln\left(\frac{(P - P_{v,w})^{3/2}}{P_{sd}^{3/2}}\right). \tag{4}$$

The first term represents the reversible potential U^0_{rev} under standard conditions, and the second term expresses the deviation from standard conditions due to variations in pressure and temperature. R is the universal gas constant, T is the temperature at which the electrochemical reaction occurs, P is the process pressure, $P_{v,w}$ is the water vapor saturation pressure, and P_{sd} is the pressure at standard conditions. It should be noted that the water vapor pressure is assumed to be equal to the water vapor saturation pressure due to the assumption of thermodynamic equilibrium between the gas and liquid phase of water. However, because of liquid injection, the water activity of the catalyst layer cannot be ignored, and this pressure may not actually be equal to the saturated water vapor pressure. Nevertheless, for the scope of this study, the saturation water vapor pressure is used. The standard reversible potential can be empirically estimated as [21,22]:

$$U^0_{rev} = 1.5184 - 1.5421 \cdot 10^{-3} \cdot T + 9.526 \cdot 10^{-5} \cdot T \cdot \ln T + 9.84 \cdot 10^{-8} \cdot T^2. \tag{5}$$

Similarly, the saturated water vapor pressure is empirically calculated as follows [23]:

$$P_{v,w} = \exp\left(81.6179 - \frac{7699.68}{T} - 10.9 \cdot \ln T + 9.5891 \cdot 10^{-3} \cdot T\right). \tag{6}$$

3.2.2. Activation overvoltage

The activation overvoltage U_{act} is caused by the reaction kinetics at the anode and cathode electrode interfaces [24,25]. It can be estimated using Eq. (7), where t_1, t_2, and t_3 are fitting model parameters associated with temperature. Similarly, s is a model parameter that represents the Tafel slope coefficient, and I is the current supplied to the stack [20]:

$$U_{act} = s \cdot \log\left(t \cdot \left(\frac{I}{A_{ef}}\right) + 1\right) = s \cdot \log\left(\left(t_1 + \frac{t_2}{T} + \frac{t_3}{T^2}\right) \cdot \left(\frac{I}{A_{ef}}\right) + 1\right). \tag{7}$$

3.2.3. Ohmic overvoltage

The ohmic overvoltage, denoted as U_{ohm}, arises from the electrical resistances present within the electrolyzer cell. It signifies the voltage drop between the anode and cathode electrodes. This drop in voltage is a consequence of the resistance of the solid material to electric current and the resistance of the liquid to the transport of ion flux. It can be estimated using Eq. (8), where r_1 and r_2 are fitting model parameters related to temperature [20]:

$$U_{ohm} = r \cdot \left(\frac{I}{A_{ef}}\right) = r_1 + r_2 \cdot T \cdot \left(\frac{I}{A_{ef}}\right). \tag{8}$$

3.3. Stack thermal model—Energy balance

The temperature of the electrolyzer stack can be estimated using the lumped-capacitance method. This method offers a straightforward approach to dynamically estimate the stack temperature over time. For an electrolyzer, this method is justified, because the heat convection from the stack to the environment is slower than the heat conduction within the body [26]. Therefore, the ordinary differential equation (ODE) for the stack temperature is formulated as follows:

$$C \cdot \frac{dT}{dt} = \dot{Q}_{gen} - \dot{Q}_{liq} - \dot{Q}_{amb} - \dot{Q}_{vap}, \tag{9}$$

where $\dot{Q}_{gen}$ represents the heat generated by overpotentials, $\dot{Q}_{liq}$ indicates the cooling caused by the colder circulating water, $\dot{Q}_{amb}$ denotes the heat loss to the ambient, and $\dot{Q}_{vap}$ represents the latent heat of vaporization.

The heat loss from the stack to the ambient is estimated as convective plus radiative heat transfer [27]:

$$\dot{Q}_{amb} = (h_{cv} + h_{rd}) \cdot A_{sur} \cdot (T_s - T_{amb}), \tag{10}$$

where h_{cv} is the convective heat transfer coefficient, and h_{rd} is the radiative heat transfer coefficient.

The thermal capacitance of the entire stack is denoted by C. It can be determined either theoretically or experimentally. In theoretical estimation, the thermal capacitance is a function of the density, heat capacity, and volume of each element that collectively forms an electrolyzer cell [15,27]. In experimental estimation, the thermal capacitance can be derived from the cooling-down data of the stack. The theoretical model of Newton's law of cooling can be fitted to the cooling-down data to estimate the thermal capacitance of the stack. For this study, the thermal capacitance is determined experimentally, and the equations for Newton's law of cooling are as follows:

$$T_s(t) = T_{amb} + (T_s(0) - T_{amb}) \cdot \exp(\frac{-t}{\tau}), \tag{11}$$

$$\tau = \frac{C}{h \cdot A_{sur}}, \tag{12}$$

$$h = h_{cv} + h_{rd}, \tag{13}$$

where T_s is the temperature of the stack, T_{amb} is the ambient temperature, and τ represents a time constant. In Eq. (13), A_{sur} stands for the surface area of the stack, and h denotes the overall heat transfer coefficient, which is the sum of the convective and radiative heat transfer coefficients.

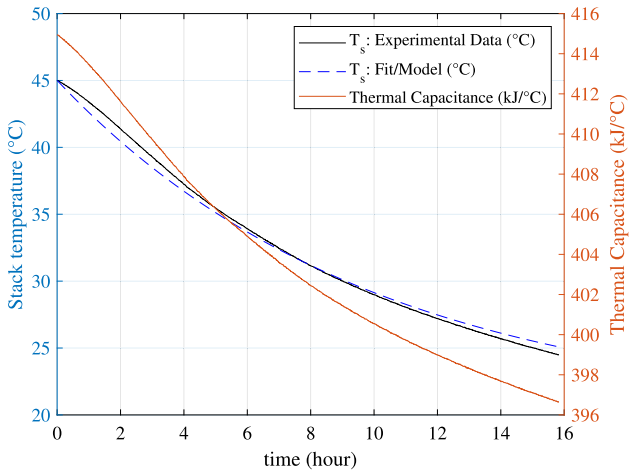

Fig. 2. Determining stack thermal capacitance by fitting experimental cooling data to the theoretical model based on Newton's law of cooling.

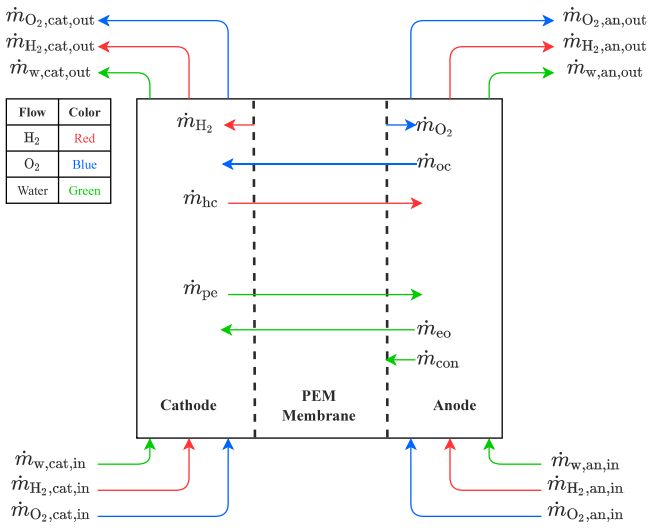

Fig. 3. Overview of mass transfer mechanisms and cell mass balance.

The fitting process is performed in MATLAB using the fminsearch function [28,29]. The results of fitting Newton's law of cooling (Eq. (11)) to the cooling-down experimental data are shown in Fig. 2. It is noteworthy that during the experiment the pumps were closed and there was no cooling by the circulating water. While the thermal capacitance exhibits some variation with stack temperature, the changes are minimal, allowing us to assume a constant value to simplify the calculations. In our scenario, the mean value of the thermal capacitance function as shown in Fig. 2 is selected as a constant for stack thermal capacitance, set at $404\,\mathrm{kJ\,°C^{-1}}$.

The heat generated by overvoltages across the entire stack is calculated as [20]:

$$\dot{Q}_{\mathrm{gen}} = N_{\mathrm{c}} \cdot (U_{\mathrm{c}} - U_{\mathrm{tn}}) \cdot I, \tag{14}$$

where N_{c} is the number of cells connected in series, and U_{tn} is the thermoneutral voltage:

$$U_{\mathrm{tn}} = \frac{\Delta H}{z \cdot F}, \tag{15}$$

where ΔH is the higher heating value (HHV) heat of reaction.

The circulating water, flowing through the heat exchangers before re-entering the stack, plays an important role in cooling down the stack. This cooling effect is estimated as follows:

$$\dot{Q}_{\mathrm{liq}} = \dot{m}_{\mathrm{w,in}} \cdot \mathrm{Cp_w} \cdot (T_{\mathrm{s}} - T_{\mathrm{w,in}}), \tag{16}$$

where $\dot{m}_{\mathrm{w,in}}$ is the total mass flow rate of water at the stack inlet, $\mathrm{Cp_w}$ is the specific heat of water ($4.18\,\mathrm{kJ\,kg^{-1}\,°C}$), and $T_{\mathrm{w,in}}$ represents the water temperature at the inlet.

According to [27,30], the convective heat transfer can be modeled as a low-velocity forced convection scenario. The Nusselt number for forced convective flow through a rectangular body can be estimated empirically, as shown in Eq. (17). For a slow-moving air flow, the Reynolds number Re is equal to 5000, and the Prandtl number Pr is 0.7. The convective heat transfer coefficient is calculated as shown in Eq. (18), where k is the thermal conductivity of the air at 20 °C, and L_{s} is the total length of the stack.

$$\mathrm{Nu} = 0.66 \cdot \mathrm{Re}^{0.675} \cdot \mathrm{Pr}^{1/3}, \tag{17}$$

$$h_{\mathrm{cv}} = \frac{Nu \cdot k}{L_{\mathrm{s}}}. \tag{18}$$

The radiative heat transfer coefficient is estimated as shown in Eq. (19), where ϵ is the emissivity of stainless steel, σ is the Stefan–Boltzmann constant, and T_{mean} is the mean temperature between the temperatures of the stack surface and the surrounding area where the stack is located. For simplification, the surrounding area temperature is assumed to be equal to the ambient temperature. The stack surface temperature is considered equal to the overall stack temperature, according to the lumped-capacitance method. This method assumes that the temperature remains uniform throughout the body.

$$h_{\mathrm{rd}} = 4 \cdot \epsilon \cdot \sigma \cdot T_{\mathrm{mean}}^{3}. \tag{19}$$

Concluding, the cooling effect resulting from water vaporization can be estimated using Eq. (20), where $\dot{m}_{\mathrm{vw,out}}$ represents the total mass flow rate of water vapor at the stack outlet, and $\lambda_{\mathrm{H_2O}}$ denotes the latent heat of vaporization ($2308\,\mathrm{kJ\,kg^{-1}}$, 80 °C) [31].

$$\dot{Q}_{\mathrm{vap}} = \dot{m}_{\mathrm{vw,out}} \cdot \lambda_{\mathrm{H_2O}}. \tag{20}$$

3.4. Mass transfer model

In water electrolysis, mass transfer occurs between the cathodic and anodic cell components, involving the transfer of both water and gas. Three methods of water transfer have been identified in the literature: (1) diffusion; (2) electroosmotic drag; and (3) water transfer due to the pressure gradient across the cell [4,32]. Gas transfer, also known as gas crossover, results from two main mechanisms: (1) convection and (2) diffusion of the product gases through the membrane. The convective mechanism is further divided into two phenomena leading to gas crossover, namely cell differential pressure and electroosmotic drag [33].

The overall cell mass balance and the mass transfer mechanisms considered in this model are illustrated in Fig. 3, where $\dot{m}_{\mathrm{H_2}}$ represents the mass flow rate of hydrogen production, $\dot{m}_{\mathrm{O_2}}$ is the mass flow rate of oxygen production, $\dot{m}_{\mathrm{hc}}$ is the mass flow rate of hydrogen crossing the anode cell compartment, $\dot{m}_{\mathrm{oc}}$ is the mass flow rate of oxygen crossing the cathode cell compartment, $\dot{m}_{\mathrm{pe}}$ indicates water transfer from the cathode to the anode due to the pressure gradient, $\dot{m}_{\mathrm{eo}}$ represents water transfer from the anode to the cathode due to electroosmotic drag, and $\dot{m}_{\mathrm{con}}$ denotes the water consumption required for the water-splitting reaction.

It should be noted that, unlike standard PEM electrolyzer cells, which receive water only on the anode half-cell for the electrochemical reaction of water splitting, our experimental setup introduced water into both half-cell compartments to improve thermal distribution within the cells and the entire stack and create a uniform temperature profile. Additionally, the hydrogen gas introduced into the anode half-cell represents recirculated impurities, and the same applies to the oxygen gas introduced into the cathode half-cell.

Based on Lin et al. [34], the uniformity of the flow field can significantly impact the performance of a PEM electrolyzer. This is why it is generally recommended to design electrolyzers to operate with uniform voltage, flow, pressure, and temperature profiles across the cells and stack.

3.4.1. Water transfer

In the process of PEM electrolysis, protons (H^+ ions) move from the anode cell compartment to the cathode through the membrane, and in this transfer, they can carry water molecules with them. This phenomenon is referred to as electroosmotic drag and is recognized as the primary mechanism for water transport in PEM cells [32]. The dragged water molar flow is estimated as:

$$\dot{n}_{eo} = n_{eo} \cdot \frac{I}{F}, \tag{21}$$

where n_{eo} is a water electroosmotic drag coefficient, and it can be empirically calculated as [4]:

$$n_{eo} = 0.016 \cdot T - 2.89556. \tag{22}$$

The molar flow of water from the cathode to the anode is also driven by the pressure effect or the pressure gradient present between the half-cells. Based on Darcy's law, the estimation of this molar flow is derived as [32,35]:

$$\dot{n}_{pe} = \frac{K_{darcy} \cdot A_m \cdot \rho_w \cdot \Delta P}{\delta_m \cdot \mu_w \cdot M_w}, \tag{23}$$

where K_{darcy} represents the membrane permeability to water ($1.58 \cdot 10^{-18}$ m^2), μ_w is the water viscosity ($1.1 \cdot 10^{-3}$ Pa s), ΔP is the pressure difference between the cathode and anode half-cells, ρ_w is the density of water [36], M_w is the molar mass of water, A_m is the membrane area, and δ_m (0.018 cm) represents the membrane thickness.

3.4.2. Gas transfer

The gas transfer process is simulated with the assistance of experimental data of H_2inO_2 impurities from the PEM plant. The recorded H_2inO_2 values during nominal and minimum current supply are fitted to Eq. (24). The fitting process is executed with the help of the fmin-search function in MATLAB [28,29]. The impurities are represented as an exponential decay function dependent on current supply, a behavior documented in the literature [37].

$$f(I) = p_1 \cdot \exp(p_2 \cdot I). \tag{24}$$

The experimental values of H_2inO_2 used for the fitting are presented in Table 2. It is also evident that there is no substantial difference between the 10 bar case and the 5 bar case. The resulting model parameters, for the 5 bar case, are 0.9889 for p_1 and −0.0013 for p_2. Additionally, the accuracy of the model is compared with experimental data, as illustrated in Fig. 4. Based on percentage deviation, the accuracy stands at 92.36%. The fit is slightly off because the model assumes the mixing of H_2inO_2 occurs instantaneously. This assumption results in a faster response of the impurities in the model compared to the slower response observed in the real operational plant, as shown in Fig. 4. However, as the precision of the mass and gas transfer is not the primary focus of this study, the accuracy achieved is considered satisfactory.

3.5. Cell mass balance

The mass balance equation for the modeled PEM cell is expressed by Eq. (25). This equation states that the rate of mass accumulation within the cell is equal to the sum of the total mass flow rate at the inlet ($\dot{m}_{in}$) and the total mass flow rate of the produced hydrogen and oxygen ($\dot{m}_{gen}$), subtracted by the total mass flow rate at the outlet ($\dot{m}_{out}$) and the consumed water ($\dot{m}_{con}$).

$$\frac{dm}{dt} = \sum \dot{m}_{in} + \sum \dot{m}_{gen} - \sum \dot{m}_{out} - \dot{m}_{con}. \tag{25}$$

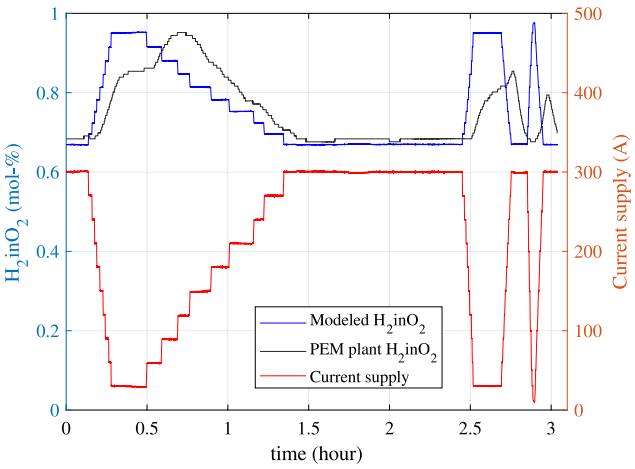

Fig. 4. Comparison of experimental H_2inO_2 data with the modeled H_2inO_2.

Table 2
Experimental values of H_2inO_2 impurities at various pressures and current supplies.

Pressure (bar)	Current supply (A)	H_2inO_2 (mol%)
5	30	0.959
5	300	0.676
10	30	0.952
10	300	0.676

The total mass flow rate at the inlet is estimated as shown in Eq. (26), where $\dot{m}_{w,cat,in}$ is the mass flow rate of water in the inlet of the cathode side, $\dot{m}_{H_2,cat,in}$ is the mass flow rate of the dissolved hydrogen gas in the inlet of the cathode side, $\dot{m}_{O_2,cat,in}$ is the mass flow rate of the dissolved oxygen gas in the inlet of the cathode side, $\dot{m}_{w,an,in}$ is the mass flow rate of water in the inlet of the anode side, $\dot{m}_{H_2,an,in}$ is the mass flow rate of the dissolved hydrogen gas in the inlet of the anode side, and $\dot{m}_{O_2,an,in}$ is the mass flow rate of the dissolved oxygen gas in the inlet of the anode side.

$$\sum \dot{m}_{in} = \dot{m}_{w,cat,in} + \dot{m}_{H_2,cat,in} + \dot{m}_{O_2,cat,in} + \dot{m}_{w,an,in} + \dot{m}_{H_2,an,in} + \dot{m}_{O_2,an,in}. \tag{26}$$

The total mass flow rate generated within the cell is calculated as illustrated in Eq. (27). This value results from the product of the hydrogen and oxygen production within the cathode and anode cell components, respectively. Thus, the total mass flow rate at the outlet is estimated according to Eq. (28):

$$\sum \dot{m}_{gen} = \dot{m}_{H_2} + \dot{m}_{O_2}, \tag{27}$$

$$\sum \dot{m}_{out} = \dot{m}_{w,cat,out} + \dot{m}_{H_2,cat,out} + \dot{m}_{O_2,cat,out} + \dot{m}_{w,an,out} + \dot{m}_{H_2,an,out} + \dot{m}_{O_2,an,out}. \tag{28}$$

3.6. System-level model methodology

The system-level process model for the PEM plant is developed within the MATLAB Simulink environment, with the corresponding diagram illustrated in Fig. 5. A total of eight MATLAB Simulink block models have been developed: two for the vertical gas–water separation vessels, two for PEM stacks A and B, and four for each heat exchanger. The pumps are not explicitly modeled because the mass flow rate after the pump is considered a model parameter, provided by the user. The

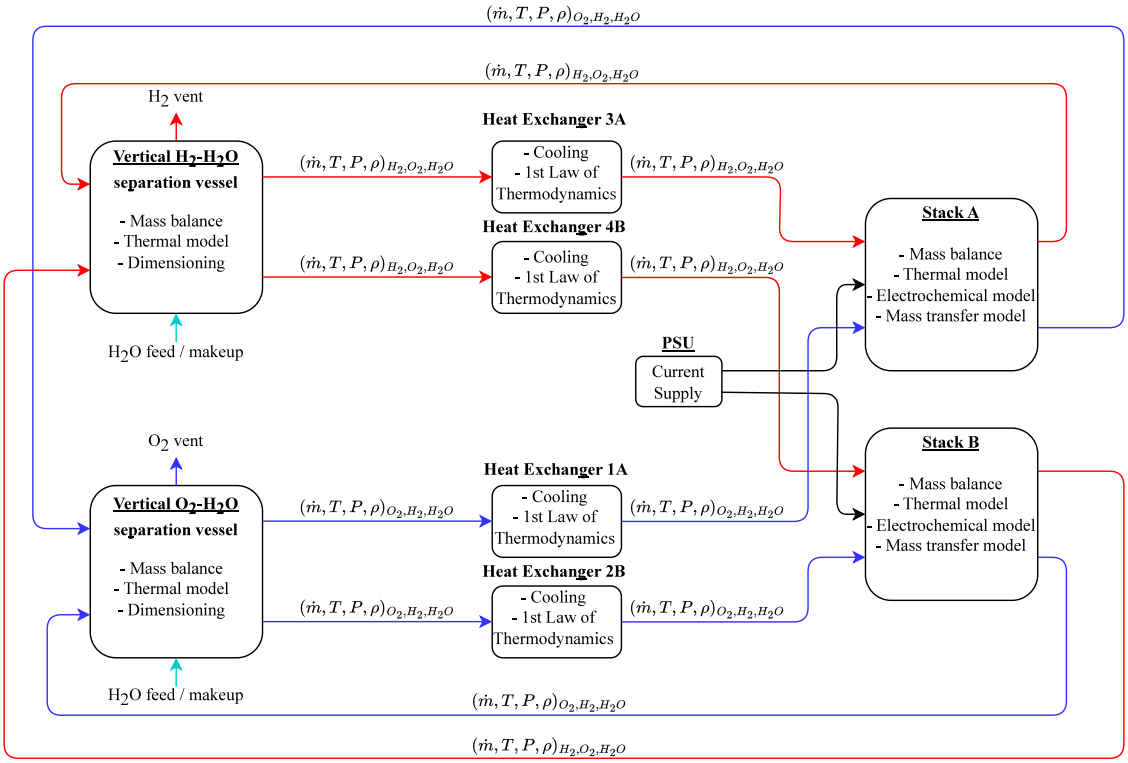

Fig. 5. MATLAB Simulink block diagram and organization of the models. The diagram depicts a system where blue-colored lines signify oxygen as the primary gas, while red-colored lines indicate hydrogen. In the Simulink model, individual signal lines are dedicated to hydrogen, oxygen, and water. However, for diagrammatic simplicity, these signals are combined into a single line, with distinct colors denoting their respective primary gases. Each block represents a MATLAB model, with the added bullet points indicating the primary methodologies used to code the specific unit operations.

MATLAB system block methodology [38] is employed for the process model. Signals are sent to each block at every time step; the blocks then perform calculations based on the signal inputs and estimate certain outputs, which are subsequently sent as inputs to the next block. Each input/output signal contains four major thermodynamic properties: mass flow rate, temperature, pressure, and density. These signals can represent hydrogen, oxygen, or water flow.

3.7. Gas–water separation vessels

The PEM plant incorporates two vertical vessels dedicated to gas–water separation: one designed for hydrogen–water separation and the other for oxygen–water separation. Each vessel is modeled individually. Each model contains its specific mass and energy balances, along with dimensioning parameters.

3.7.1. Mass balance

The mass balance equation for the vertical gas–water separation vessels is presented in Eq. (29). This equation states that the rate of mass accumulation within the vessel equals the total mass flow rate at the inlet minus that at the outlet. The outlet, in turn, is divided into two ports: the downer vessel outlet and the upward vessel outlet.

$$\frac{dm}{dt} = \sum \dot{m}_{\text{in}} - \left(\sum \dot{m}_{\text{out,down}} + \sum \dot{m}_{\text{out,up}}\right). \tag{29}$$

The total mass flow rate at the inlet is shown in Eq. (30), where $\dot{m}_{H_2,A,in}$ is the inlet mass flow rate of hydrogen coming from stack A, $\dot{m}_{H_2,B,in}$ is the inlet mass flow rate of hydrogen coming from stack B, $\dot{m}_{O_2,A,in}$ and $\dot{m}_{O_2,B,in}$ stand for the inlet mass flow rates of oxygen coming from stacks A and B, respectively, $\dot{m}_{w,A,in}$ and $\dot{m}_{w,B,in}$ are the inlet mass flow rates of water coming from stacks A and B, respectively, and finally, $\dot{m}_{mp,in}$ represents the inlet mass flow rate of makeup water.

$$\sum \dot{m}_{\text{in}} = \dot{m}_{H_2,A,in} + \dot{m}_{H_2,B,in} + \dot{m}_{O_2,A,in} + \dot{m}_{O_2,B,in} + \dot{m}_{w,A,in} + \dot{m}_{w,B,in} + \dot{m}_{mp,in}. \tag{30}$$

The total outlet mass flow rate at the downer of the vessel is expressed in Eq. (31), while the total outlet mass flow rate at the upward of the vessel is presented in Eq. (32). These mass balances are solved using separation efficiencies, where $\eta_{s,l}$ denotes the separation efficiency of water, η_{s,H_2} represents the separation efficiency of hydrogen gas, and η_{s,O_2} signifies the separation efficiency of oxygen gas. These separation efficiencies serve as model parameters, aiding in either fitting the model with experimental data of H_2inO_2 and O_2inH_2 impurities or establishing assumptions regarding the amount of oxygen and hydrogen dissolved in the water. Another approach to this is to model the dissolution of hydrogen and oxygen in water to determine the amount of dissolved gas molecules leaving the vessel through the downer and upward outlets [17]. However, these detailed models are beyond the scope of this study.

$$\sum \dot{m}_{\text{out,down}} = (\dot{m}_{w,A,in} + \dot{m}_{w,B,in} + \dot{m}_{mp,in}) \cdot \eta_{s,l} + (\dot{m}_{H_2,A,in} + \dot{m}_{H_2,B,in}) \cdot (1 - \eta_{s,H_2}) + (\dot{m}_{O_2,A,in} + \dot{m}_{O_2,B,in}) \cdot (1 - \eta_{s,O_2}), \tag{31}$$

$$\sum \dot{m}_{\text{out,up}} = (\dot{m}_{w,A,in} + \dot{m}_{w,B,in} + \dot{m}_{mp,in}) \cdot (1 - \eta_{s,l}) + (\dot{m}_{H_2,A,in} + \dot{m}_{H_2,B,in}) \cdot \eta_{s,H_2} + (\dot{m}_{O_2,A,in} + \dot{m}_{O_2,B,in}) \cdot \eta_{s,O_2}. \tag{32}$$

3.7.2. Vessel thermal model—Energy balance

The lumped capacitance method is used to transiently estimate the thermal behavior of the vessels, as shown in Eq. (33). In this equation,

the thermal capacitance of the vessel is expressed as C_v. Additionally, $\dot{Q}_{in}$ represents the total incoming heat resulting from the combined flows of water, hydrogen, and oxygen at the inlet, while $\dot{Q}_{out}$ signifies the total heat exiting the system with the outflowing water, hydrogen, and oxygen. Sensible heat transfer equations are used to estimate both the total incoming and outflowing heat. Furthermore, $\dot{Q}_{amb}$ represents the heat dissipated to the ambient environment from the vessel and is calculated as free convective heat transfer of cylinder. Finally, $\dot{Q}_{mp}$ denotes the cooling of the vessel caused by the colder makeup water inlet flow.

$$C_v \cdot \frac{dT}{dt} = \dot{Q}_{in} - \dot{Q}_{out} - \dot{Q}_{amb} - \dot{Q}_{mp}. \tag{33}$$

The lumped capacitance method operates under the assumption of uniform temperature within the system. Consequently, the vessel temperature equals the temperature of the outflowing streams. Hence, Q_{outlet} is consistently zero because no higher temperature flow exits the vessel.

The thermal capacitance of the vessel is determined by considering the total volume occupied by water within the vessel, and it can be calculated as follows:

$$C_v = \rho_w \cdot Cp_w \cdot V_L, \tag{34}$$

where ρ_w is the density of water, Cp_w is the specific heat capacity of water, and V_L is the total volume of the vessel that is occupied by water.

3.8. Heat exchangers

The heat transfer between the hot and cold tubes was assumed to occur in parallel, and the heat exchanger was modeled as an ideal component. In this setup, the heat transfer phenomena can be explained using the principles of the first law of thermodynamics [39]. Consequently, the energy balance and the rate of heat transfer can be characterized as:

$$q = \dot{m}_h \cdot Cp_w \cdot (T_{h,in} - T_{h,out}) = \dot{m}_{cd} \cdot Cp_w \cdot (T_{cd,in} - T_{cd,out}), \tag{35}$$

where $\dot{m}_h$ represents the mass flow rate of the hot water from the plant process circulation, and $\dot{m}_{cd}$ denotes the mass flow rate of the cold cooling water. $T_{h,in}$, $T_{h,out}$, $T_{cd,in}$, and $T_{cd,out}$ correspond to the temperatures of the hot water at the inlet, hot water at the outlet, cold water at the inlet, and cold water at the outlet, respectively.

3.8.1. Closed-loop temperature control logic

During the simulation, the temperature of the stack is controlled by adjusting the process temperature using an analytical solution within the heat exchanger sub-model. The temperature set-point and the cooling water temperature are used as initial model parameters. The analytical solution estimates the temperature of the liquid at the outlet of the heat exchanger based on the given temperature set-point and is determined as follows:

$$\Delta T_{cd} = |T - T_{cw}|, \tag{36}$$

$$S = \Delta T_{cd} \cdot Cp_w, \tag{37}$$

$$\Delta T_1 = T - T_{SP}, \tag{38}$$

$$Q_{sec} = \Delta T_1 \cdot Cp_w \cdot \dot{m}_h, \tag{39}$$

$$\dot{m}_{cd} = \frac{Q_{sec}}{S}, \tag{40}$$

$$Q_{sec,new} = S \cdot \dot{m}_{cd}, \tag{41}$$

$$\Delta T_2 = \frac{Q_{sec,new}}{\dot{m}_h \cdot Cp_w}, \tag{42}$$

$$T_{out} = T - \Delta T_2, \tag{43}$$

where ΔT_{cd} is the absolute temperature difference between the process temperature T and the cooling water temperature T_{cw}, S is the specific energy required to cool the process temperature, ΔT_1 is the temperature difference between the process temperature and set-point temperature, Q_{sec} is the amount of heat transferred from the primary leg to the secondary leg within the heat exchanger, and T_{out} is temperature of the primary liquid (hot side) at the outlet of the heat exchanger.

4. Results

As outlined in Section 1, one the primary objectives of this study is to develop a verified dynamic mass and energy balance model for a PEM plant. This model will serve as a foundation for future investigations, analyzing the potential of PEM plants connected to RES, either as standalone units focused on green hydrogen production or as components within PtX systems. To verify the model, experiments were conducted using a real PEM plant situated in Karlsruhe Institute of Technology (KIT), Germany. Throughout these experiments, operational transient data were recorded, including stack power, total stack voltage, total stack current supply, liquid temperatures at the anode and cathode inlets and outlets of the stack, temperatures of individual cells, mass flow rates of all four pumps, hydrogen production rate, process pressures at six different locations, H_2inO_2 impurities, and voltage across each cell. The experimental data were sampled at one-second time steps.

4.1. Model verification

The verification and comparison of the model was performed at three separate levels, namely electrochemical model, stack temperature, and hydrogen production. To model the electrochemical behavior, the real polarization curve was compared with the modeled one, as shown in Fig. 6. The polarization curve of the actual PEM plant was obtained at three different temperatures: 52.2 °C, 56 °C, and 58.7 °C. The MATLAB fminsearch function was employed to fit the modeled polarization curve. The polarization curve fitting process followed the steps outlined by Ulleberg et al. [20]. At first, each individual measured polarization curve underwent an initial fitting without considering temperature dependence. This involved fitting Eq. (4) and the first sections of Eqs. (7) and (8) while estimating the model parameters r and t for each case. Subsequently, linear and quadratic curve fitting was applied to parameters r and t, respectively, to derive preliminary estimations of r_i and t_i, as demonstrated in the second parts of Eqs. (7) and (8). Finally, these preliminary estimations were validated to ensure that they follow the temperature and pressure dependence behavior, and an overall curve fitting of Eq. (2) was performed. The resulting values of the electrochemical model parameters are presented in Table 3. For model replication, note that the fitting was performed at the stack level, and the use of the provided model parameter values estimates the stack voltage and overvoltages.

In addition to verifying the electrochemical model, the dynamic thermal behavior of the modeled stack was compared with that of the real PEM plant, as shown in Fig. 7. The thermal model demonstrated satisfactory performance in predicting the actual dynamic stack temperature behavior, with a percentage deviation accuracy of 98.32%, average relative error of 1.75%, and root mean square error (RMSE) of 1.2075 °C. These results allowed an analysis of the energy balance within the stack, as illustrated in Fig. 8. The analysis was performed for both stacks A and B, producing identical results because the stacks are identical, and thus, only stack A is demonstrated and analyzed. The stack temperature was maintained constant at 60 °C, and the simulation was run until reaching a steady state for each current supply ranging from 0 A to 300 A. The only heat source within the stack arises from

Table 3
Model parameters used in the model.

Sub-model	Variable	Value	Unit	Equation
Electrochemical	r_1	3.57	$\Omega\,cm^2$	Eq. (8)
Electrochemical	r_2	0.46	$\Omega\,cm^2\,°C^{-1}$	Eq. (8)
Electrochemical	t_1	198.77	$cm^2\,A^{-1}$	Eq. (7)
Electrochemical	t_2	−41319.46	$cm^2\,°C\,A^{-1}$	Eq. (7)
Electrochemical	t_3	2168180.07	$cm^2\,°C^2\,A^{-1}$	Eq. (7)
Electrochemical	s	7.09	V	Eq. (7)
Gas transfer	p_1	0.9889	–	Eq.(24)
Gas transfer	p_2	−0.0013	–	Eq.(24)
Vessel mass balance	$\eta_{s,l}$	1	–	Eq. (31) and Eq. (32)
Vessel mass balance	η_{s,O_2}	0.99	–	Eq. (31) and Eq. (32)
Vessel mass balance	η_{s,H_2}	0.99	–	Eq. (31) and Eq. (32)

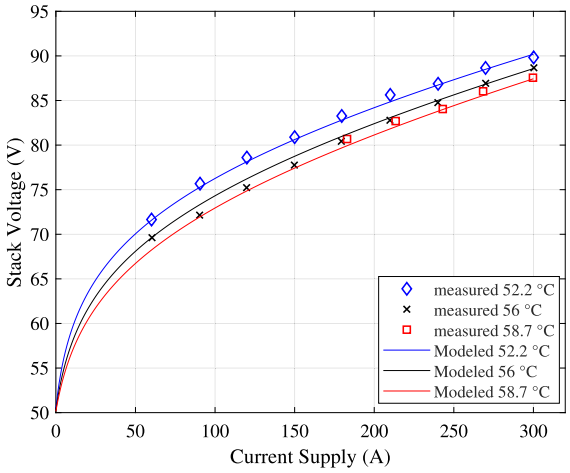

Fig. 6. Comparison of the modeled and measured polarization curves.

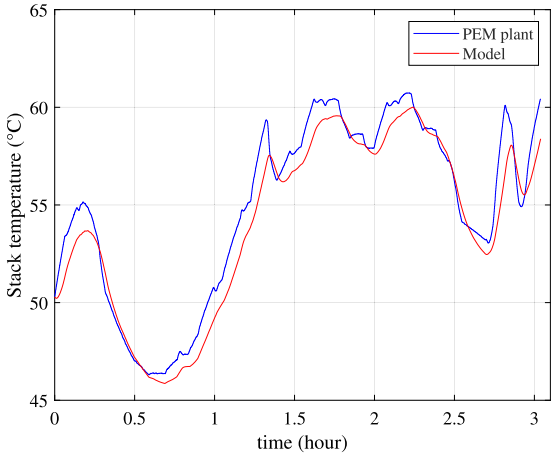

Fig. 7. Verification of the thermal model. The measured current supply, recorded at one-second intervals, was used as the input for the process model. The resulting stack temperatures from the model are compared with the values measured from the PEM plant. The stack temperature is recorded under the same current supply conditions presented in Fig. 4.

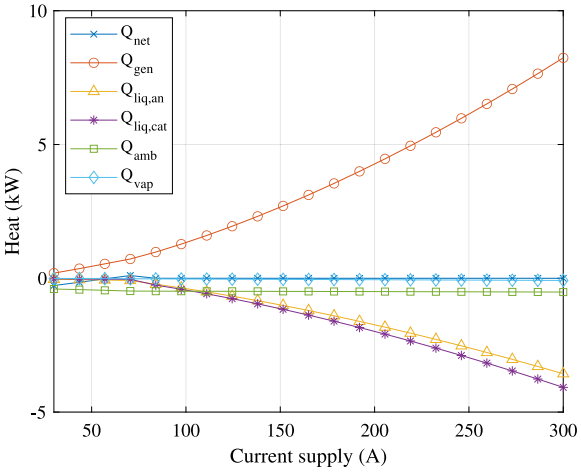

Fig. 8. Energy balance analysis of stack A. Here, $\dot{Q}_{net}$ represents the equilibrium of the energy balance between the energy entering and leaving the system, which must always be zero.

the heat generated by overvoltages ($\dot{Q}_{gen}$), which increase gradually with current supply up to 8.2 kW at nominal load. The lowest means of cooling is the vaporization of water ($\dot{Q}_{vap}$), which increased with current supply from 0.002 kW to 0.07 kW. The impact of vaporization decreases with an increase in pressure; in particular, at pressures above atmospheric pressure it becomes less significant. Heat loss to the ambient environment ($\dot{Q}_{amb}$) was constant 0.5 kW across the whole current supply range, ranking second in magnitude. Lastly, cooling by circulating water increased with current supply and was estimated to be 3.6 kW for the anodic side ($\dot{Q}_{liq,an}$) and 4.1 kW for the cathodic side ($\dot{Q}_{liq,cat}$) at nominal load. The amount of heat transferred from the stack to the cooling water is lower for the anodic side compared with the cathodic side. This is due to the fact that the overall mass flow rate of water entering the anodic side is lower compared with the cathodic side. The pump mass flow rates for the case are shown in Table 4.

The final model verification focused on hydrogen production. As shown in Fig. 9, the modeled hydrogen production closely matched the measurements from the PEM plant. A minimal deviation was observed, primarily due to the submodel of H_2inO_2 impurities. As shown in Fig. 4, the model tends to overestimate the amount of hydrogen gas lost as impurities to the oxygen line. Nevertheless, despite this slight inaccuracy, the process model can predict the measured hydrogen production with a percentage deviation accuracy of 98.64%, average relative error of 1.36%, and RMSE of 0.15 Nm^3/h.

4.2. Analysis of stack and heat exchangers

The SECs of stacks A and B were analyzed across various stack temperatures within a current supply range. The results were obtained by running the process model until a steady state was reached for each current supply, ranging from 30 A to 300 A. The initial design parameters used for simulation and data retrieval are given in Table 4. Fig. 10 shows the SEC of stack A. Both stacks were operated with identical loads, and no significant differences were observed. Hence, only stack A was analyzed for simplification.

It is evident that as the stack temperature increases, the SEC decreases. This trend comes primarily from the decrease in activation overvoltage with a temperature rise due to favorable reaction kinetics,

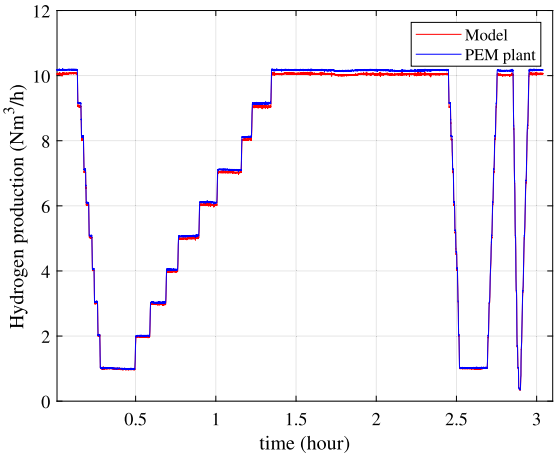

Fig. 9. Comparison of the modeled hydrogen production with that measured from the PEM plant. The hydrogen production is recorded under the same current supply conditions presented in Fig. 4.

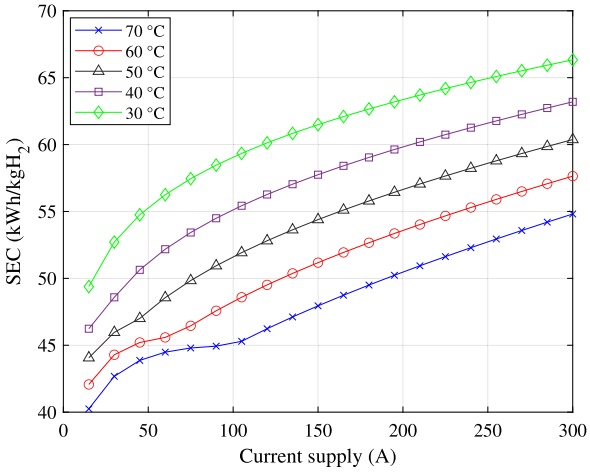

Fig. 10. Analysis of stack A SEC at various temperatures. At 50 °C, 60 °C, and 70 °C, and in lower current supply ranges, note that the stack temperature did not reach the set point temperature because of insufficient heat from the stack overvoltages.

thereby enhancing the energy efficiency of the stack [40]. On the other hand, the ohmic overvoltage increases with a temperature rise, although with a lesser impact compared with the decrease in activation overvoltage. As a result, the overall polarization curve decreases with a temperature increase. This phenomenon is also illustrated in Fig. 6.

Fig. 10 also illustrates that at lower current densities and higher temperatures, the SEC shows an upside-down U-shape, indicating a loss of energy efficiency during partial load operation. This occurs because the stack overvoltages (heat source) are not sufficient to raise the temperature at 50 °C, 60 °C, and 70 °C, respectively, during a low current supply. In such cases, reducing the mass flow rate of the incoming circulating water or installing external heating may enhance the energy efficiency at partial loads. However, implementing such an installation should be optimized and evaluated to determine its economic viability. This outcome might be an important consideration during RES connected to PEM plants. In these cases, electrolyzer plants might operate at partial loads for extended periods due to the intermittency of renewable electricity production [41].

The heat exchangers were analyzed to determine the precise amount of waste heat transferred from the primary circulation leg to the secondary. As shown in Fig. 11, the heat transferred increases with an increase in current owing to the rise in overvoltages. Consequently,

Table 4
Initial design parameters used for the simulations.

Parameter	Variable	Value	Unit
Pump 1A mass flow rate	$\dot{m}_{pp,1A}$	1163	kg h^{-1}
Pump 2B mass flow rate	$\dot{m}_{pp,2B}$	1255	kg h^{-1}
Pump 3A mass flow rate	$\dot{m}_{pp,3A}$	1329	kg h^{-1}
Pump 4B mass flow rate	$\dot{m}_{pp,4B}$	1191	kg h^{-1}
Initial stack temperature	$T_{s,init}$	25	°C
Ambient temperature	T_{amb}	20	°C
Makeup water temperature	T_{mp}	25	°C
Vessel diameter	D_{vessel}	0.1862	m
Vessel height	H_{vessel}	0.5585	m
Set point of heat exchangers	T_{SP}	60	°C
Cooling water temperature	T_{cw}	20	°C

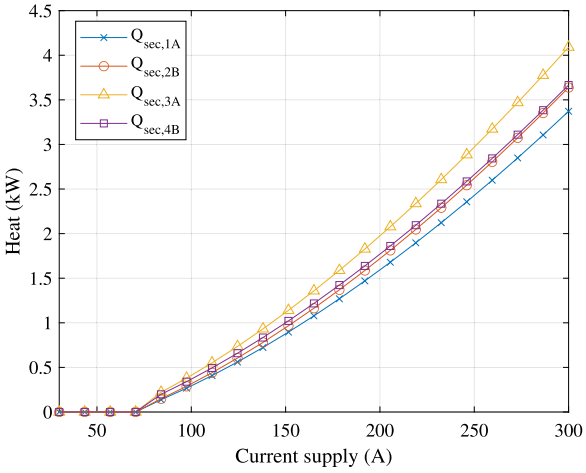

Fig. 11. Heat transfer to the secondary leg through the heat exchangers.

more heat extraction is required from the primary circulation as the stack approaches its nominal load. It is also noteworthy that until 70 A of current supply, no heat is transferred to the secondary leg. This is due to the same reason as the upside-down U-shape observed in Fig. 10. Essentially, the overvoltages are not sufficiently high to elevate the temperature to the set point, which was 60 °C for the simulation case.

Furthermore, it is observed that, in general, a substantial amount of heat is transferred during the heat exchange process. Specifically, during nominal load, heat exchanger 1A transferred 3.3 kW of heat, heat exchanger 2B 3.6 kW, heat exchanger 3A 4.1 kW, and heat exchanger 4B 3.7 kW. Broadly, the amount of heat transferred by each heat exchanger can be controlled by adjusting the pump mass flow rate. Currently, for industrial-scale water electrolyzers, this waste heat is not generally utilized; however, it could serve as valuable heat for nearby residential areas.

4.3. Power distribution across the plant

The distribution of the power supplied to stacks A and B is shown in Fig. 12. In the diagram, yellow indicates electrical power, purple represents chemical power, and red denotes thermal power. It can be observed that out of the total of 52 kW supplied to the stack, 35.6 kW is converted into hydrogen, with only 0.04 kW lost to gas impurities, leaving the remainder as end-product hydrogen, ready for storage and utilization. On the other hand, 16.4 kW of the total supplied power is lost to overvoltages and is dissipated as heat. Heat exchangers 1A, 2B, 3A, and 4B extract a total of 14.7 kW of heat, while 1.15 kW is lost to the ambient environment from the stacks and the gas–liquid separation vessels. Additionally, 0.15 kW is lost due to the latent heat of vaporization, and 0.4 kW is cooled through the introduction of cold makeup water.

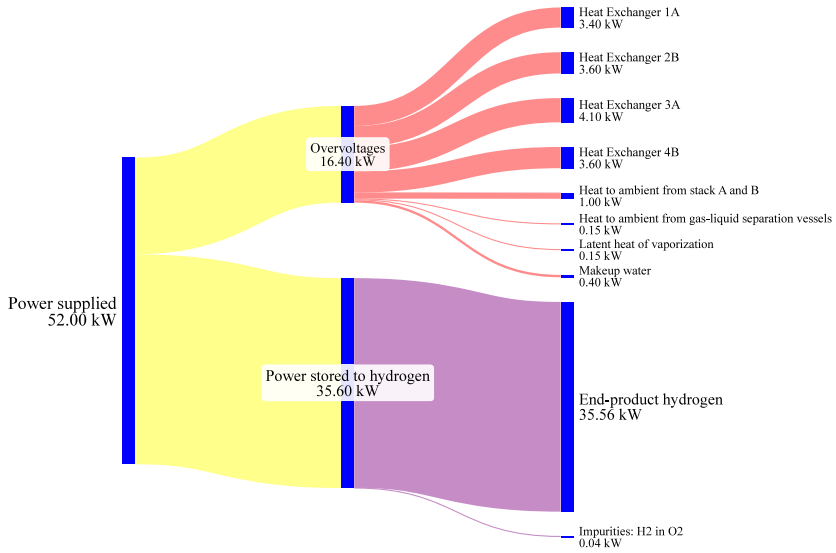

Fig. 12. Sankey diagram illustrating the distribution of power supplied to stacks A and B across the plant.

In closer analysis and in combination with previous research [15], several factors can influence the hydrogen production (end-line) and energy efficiency of a commercial or industrial-scale electrolyzer plant: (1) stack overvoltages, (2) stack shunt currents, (3) hydrogen impurities lost on the oxygen side, and (4) hydrogen burned in deoxidizer units. Our study shows that, unlike alkaline water electrolyzers [15], PEM electrolyzers do not exhibit any shunt current losses. Additionally, the amount of hydrogen lost to the oxygen side and burned in deoxidizer units is a very small fraction of the total generated. Therefore, as shown in Fig. 12 and supported by previous studies, the energy efficiency of the PEM electrolyzer stack and plant is significantly influenced by the overvoltage losses. Thus, to improve efficiency, the primary focus should be on reducing the polarization curve (UI) of the stack [42].

Fig. 12 examines the electrical power supplied to the stack and its utilization. Specifically, it addresses how much of the supplied current to the stack is lost to overvoltages, how much is converted into hydrogen, and generally how the current is distributed, converted and utilized throughout the plant process. It should be noted that this analysis excludes the energy consumed to power up the four pumps and the water purification system.

5. Conclusions

In this work, a parameter-adjustable dynamic mass and energy balance process model of a 50 kW PEM electrolyzer plant was developed using MATLAB system blocks within the Simulink environment and validated with experimental data from an analogous PEM plant. The process model comprises models for the stack, gas–liquid separation vessel, and heat exchangers. The stack model integrates electrochemical, thermal, and mass transfer submodels, while the gas–liquid separation vessel model incorporates mass balance and thermal submodels. The heat exchangers are modeled as ideal components, and heat transfer phenomena are estimated using the principles of the first law of thermodynamics.

The verification and comparison was performed at three different levels, namely electrochemical, thermal, and hydrogen production. Fitting of the electrochemical model was used to match the real polarization curve with the modeled one. The polarization curve fitting was performed at various temperatures, and the resulting model parameters were provided. In addition, the thermal behavior of the modeled stack showed excellent agreement with the real case, with a percentage deviation accuracy of 98.32%. Similarly, the comparison of hydrogen production between the real and modeled cases matched with the percentage deviation accuracy of 98.64%.

The stack SEC analysis in steady-state conditions for various temperatures showed that a higher stack temperature can enhance the SEC of the stack. Additionally, the study showed that within low current supply ranges the heat generated by overpotentials was not sufficient to increase the temperature of the stack to the set point value. Thus, in partial load operation, the stack can lose efficiency because of colder conditions.

The stack heat balance analysis in steady-state conditions showed that the latent heat of vaporization and heat dissipation to the ambient environment played a minor role in the cooling of the stack. On the other hand, the circulating water to the anode and cathode carried away most of the generated heat, which was primarily transferred to the secondary leg through the heat exchangers. In addition, a Sankey diagram showed the distribution of power supplied to the stacks across the plant. Out of the total of 52 kW supplied to stacks A and B, 35.6 kW became hydrogen gas, while the remaining 16.4 kW was dissipated as heat caused by overvoltages.

In conclusion, the paper presented a validated dynamic process model to predict the electrochemical, thermal, and hydrogen production behavior of a 50 kW PEM plant, incorporating all necessary peripheral components of the system. Future studies that integrate the model with RES as a standalone unit or as part of a PtX scheme can provide valuable insights.

CRediT authorship contribution statement

Georgios Sakas: Writing – review & editing, Writing – original draft, Visualization, Validation, Software, Resources, Project administration, Methodology, Investigation, Formal analysis, Data curation, Conceptualization. **Philipp Rentschler:** Writing – review & editing, Resources, Formal analysis, Data curation, Conceptualization. **Antti Kosonen:** Writing – review & editing, Supervision, Project administration, Funding acquisition, Conceptualization. **Peter Holtappels:** Writing – review & editing, Supervision, Funding acquisition, Formal analysis, Conceptualization. **Vesa Ruuskanen:** Writing – review & editing, Supervision, Formal analysis, Conceptualization. **Pertti Kauranen:** Writing – review & editing, Supervision, Formal analysis, Conceptualization. **Jero Ahola:** Writing – review & editing, Supervision, Funding acquisition, Formal analysis, Conceptualization. **Roland Dittmeyer:** Writing – review & editing, Supervision.

Declaration of Generative AI and AI-assisted technologies in the writing process

During the preparation of this work the authors used Grammarly, QuillBot and ChatGPT in order to improve the grammar and readability of the text. After using these tools/services, the authors reviewed and edited the content as needed and take full responsibility for the content of the publication.

Declaration of competing interest

The authors declare that they have no known competing financial interests or personal relationships that could have appeared to influence the work reported in this paper.

Acknowledgments

Business Finland is acknowledged for the main financial support of the Bio-CCU project. Dr. Hanna Niemelä is also thanked for her assistance in language revision, and improving the grammar and readability of the text.

Data availability

The data that has been used is confidential.

References

[1] Green hydrogen for sustainable industrial development: A policy toolkit for developing countries, Tech. rep., International Renewable Energy Agency (IRENA) and the German Institute of Development and Sustainability (IDOS).
[2] Buttler A, Spliethoff H. Renew Sustain Energy Rev 2018;82:2440–54. http://dx.doi.org/10.1016/j.rser.2017.09.003.
[3] Olivier P, Bourasseau C, Bouamama PB. Renew Sustain Energy Rev 2017;78:280–300. http://dx.doi.org/10.1016/j.rser.2017.03.099.
[4] Yigit T, Selamet OF. Int J Hydrog Energy 2016;41(32):13901–14. http://dx.doi.org/10.1016/j.ijhydene.2016.06.022.
[5] Espinosa-López M, Darras C, Poggi P, Glises R, Baucour P, Rakotondrainibe A, et al. Renew Energy 2018;119:160–73. http://dx.doi.org/10.1016/j.renene.2017.11.081.
[6] Ni M, Leung MK, Leung DY. Energy Convers Manage 2008;49(10):2748–56. http://dx.doi.org/10.1016/j.enconman.2008.03.018.
[7] Ioroi T, Yasuda K, Siroma Z, Fujiwara N, Miyazaki Y. J Power Sources 2002;112(2):583–7. http://dx.doi.org/10.1016/S0378-7753(02)00466-4.
[8] Hancke R, Bujlo P, Holm T, Ulleberg Ø. J Power Sources 2024;601:234271. http://dx.doi.org/10.1016/j.jpowsour.2024.234271.
[9] Pfennig M, Schiffer B, Clees T. Int J Hydrog Energy 2024. http://dx.doi.org/10.1016/j.ijhydene.2024.04.335, S0360319924016471.
[10] Solanki J, Wallmeier P, Böcker J, Averberg A, Fröhleke N. IET Power Electron 2015;8(6):1068–80. http://dx.doi.org/10.1049/iet-pel.2014.0533.
[11] Hysa G, Ruuskanen V, Kosonen A, Niemelä M, Aarniovuori L, Guilbert D, et al. J Power Sources 2023;574:233108. http://dx.doi.org/10.1016/j.jpowsour.2023.233108.
[12] Järvinen L, Puranen P, Kosonen A, Ruuskanen V, Ahola J, Kauranen P, et al. Int J Hydrog Energy 2022;47(75):31985–2003. http://dx.doi.org/10.1016/j.ijhydene.2022.07.085.
[13] Ibáñez-Rioja A, Sakas G, Järvinen L, Puranen P. In: Sguarezi Filho AJ, Jacomini RV, Capovilla CE, Casella IRS, editors. Smart grids—renewable energy, power electronics, signal processing and communication systems applications. Green energy and technology, Cham: Springer International Publishing; 2024, p. 37–72. http://dx.doi.org/10.1007/978-3-031-37909-3_2.
[14] Huusari L. Analysis of phase separator design criteria using computational fluid dynamics [Master's thesis], Lappeenranta, Finland: LUT University; 2015.
[15] Sakas G, Ibáñez-Rioja A, Ruuskanen V, Kosonen A, Ahola J, Bergmann O. Int J Hydrog Energy 2022;47(7):4328–45. http://dx.doi.org/10.1016/j.ijhydene.2021.11.126.
[16] Koponen J. Energy efficient hydrogen production by water electrolysis (Ph.D. thesis), Lappeenranta, Finland: LUT University; 2020.
[17] Sakas G, Ibáñez-Rioja A, Pöyhönen S, Järvinen L, Kosonen A, Ruuskanen V, et al. Appl Energy 2024;359:122732. http://dx.doi.org/10.1016/j.apenergy.2024.122732.
[18] Hine F. Electrochemical engineering. John Wiley & Sons, Inc; 2018.
[19] Hu S, Guo B, Ding S, Yang F, Dang J, Liu B, et al. Appl Energy 2022;327:120099. http://dx.doi.org/10.1016/j.apenergy.2022.120099.
[20] Ulleberg O. Int J Hydrog Energy 2003;28(1):21–33. http://dx.doi.org/10.1016/S0360-3199(02)00033-2.
[21] García-Valverde R, Espinosa N, Urbina A. Int J Hydrog Energy 2012;37(2):1927–38. http://dx.doi.org/10.1016/j.ijhydene.2011.09.027.
[22] LeRoy RL, Bowen CT, LeRoy DJ. J Electrochem Soc 1980;127(9):1954–62. http://dx.doi.org/10.1149/1.2130044.
[23] Gambou F, Guilbert D, Zasadzinski M, Rafaralahy H. Energies 2022;15(9):3452. http://dx.doi.org/10.3390/en15093452.
[24] Ahmadi P, Dincer I, Rosen MA. Int J Hydrog Energy 2013;38(4):1795–805. http://dx.doi.org/10.1016/j.ijhydene.2012.11.025.
[25] Sun M, Zhang Y, Liu L, Nian X, Zhang H, Duan L. Appl Energy 2025;377:124636. http://dx.doi.org/10.1016/j.apenergy.2024.124636.
[26] Incropera FP, DeWitt DP. Fundamentals of heat and mass transfer. 2006.
[27] Tiktak WJ. Heat management of PEM electrolysis: A study on the potential of excess heat from mediumto largescale PEM electrolyisis and the performance analysis of a dedicated cooling system. TU Deft; 2019.
[28] Lagarias JC, Reeds JA, Wright MH, Wright PE. SIAM J Optim 1998;9(1):112–47. http://dx.doi.org/10.1137/S1052623496303470.
[29] MATLAB fminsearch, https://se.mathworks.com/help/matlab/ref/fminsearch.html.
[30] Mills A. In: Always learning, second ed.. Pearson; 2014.
[31] Dieguez P, Ursua A, Sanchis P, Sopena C, Guelbenzu E, Gandia L. Int J Hydrog Energy 2008;33(24):7338–54. http://dx.doi.org/10.1016/j.ijhydene.2008.09.051.
[32] Awasthi A, Scott K, Basu S. Int J Hydrog Energy 2011;36(22):14779–86. http://dx.doi.org/10.1016/j.ijhydene.2011.03.045.
[33] Trinke P, Haug P, Brauns J, Bensmann B, Hanke-Rauschenbach R, Turek T. J Electrochem Soc 2018;165(7):F502–13. http://dx.doi.org/10.1149/2.0541807jes.
[34] Lin R, Lu Y, Xu J, Huo J, Cai X. Appl Energy 2022;326:120011. http://dx.doi.org/10.1016/j.apenergy.2022.120011.
[35] Marangio F, Santarelli M, Cali M. Int J Hydrog Energy 2009;34(3):1143–58. http://dx.doi.org/10.1016/j.ijhydene.2008.11.083.
[36] Kell GS. J Chem Eng Data 1975;20(1):97–105. http://dx.doi.org/10.1021/je60064a005.
[37] Haug P, Koj M, Turek T. Int J Hydrog Energy 2017;42(15):9406–18. http://dx.doi.org/10.1016/j.ijhydene.2016.12.111.
[38] MATLAB system block - MATLAB & simulink - mathworks nordic, https://se.mathworks.com/help/simulink/ug/what-is-matlab-system-block.html.
[39] Vepsäläinen A, Pitkänen J, Hyppänen T. Fundamentals of heat transfer. Lappeenranta University of Technology; 2012.
[40] Hourng LW, Tsai TT, Lin MY. IOP Conf Ser: Earth Environ Sci 2017;93:012035. http://dx.doi.org/10.1088/1755-1315/93/1/012035.
[41] Sakas G, Ibáñez-Rioja A, Pöyhönen S, Kosonen A, Ruuskanen V, Kauranen P, et al. Renew Energy 2024;225:120266. http://dx.doi.org/10.1016/j.renene.2024.120266.
[42] Carmo M, Fritz DL, Mergel J, Stolten D. Int J Hydrog Energy 2013;38(12):4901–34. http://dx.doi.org/10.1016/j.ijhydene.2013.01.151.